Third-order exciton-correlation and nonlinear cavity-polariton effects in semiconductor microcavities

N. H. Kwong,[1] R. Takayama,[1] I. Rumyantsev[2] M. Kuwata-Gonokami,[3] and R. Binder[2]
[1]*Cooperative Excitation Project, ERATO, Japan Science and Technology Corporation, Optical Sciences Center, University of Arizona, Tucson, Arizona 85721*
[2]*Optical Sciences Center, University of Arizona, Tucson, Arizona 85721*
[3]*Cooperative Excitation Project, ERATO, Japan Science and Technology Corporation, Department of Applied Physics, University of Tokyo, 7-3-1 Hongo, Bunkyo-ku, Tokyo 113-8656, Japan*
(Received 29 December 2000; revised manuscript received 13 March 2001; published 27 June 2001)

We present a microscopic theory of the coherent third-order ($\chi^{(3)}$) optical response of semiconductor quantum well microcavities, specialized to the four-wave-mixing configuration in the spectral vicinity of the lowest exciton frequency. The theory is that of a quantum-mechanical many-electron system dipole coupled to a classical radiation field. The many-electron dynamics is treated within the dynamics-controlled-truncation formalism restricted to the 1*s*-exciton subspace. Within this limitation, all Coulomb correlation effects are included, resulting in an effective theory of (virtual) exciton-polariton scattering. Good quantitative agreement of the theory is obtained in comparison to the experiments reported by Gonokami *et al.*, Phys. Rev. Lett. **79**, 1341 (1997). This comparison reveals the signatures of both the bound biexciton and the exciton-exciton scattering (continuum) correlations. Furthermore, a proper calculation of the scattering correlations is shown to be important: each of two common approximations, the Markov and the second Born, results in clear discrepancies from the data.

DOI: 10.1103/PhysRevB.64.045316 PACS number(s): 78.47.+p, 71.35.Gg, 05.30.Jp, 34.50.−s

I. INTRODUCTION

Semiconductor microcavities are the focus of many current research efforts. In the linear optical regime they exhibit interesting similarities and differences to empty and atomic microcavities (see, e.g., Ref. 1), such as normal mode splitting (see, e.g., Ref. 2, and for a recent review see Ref. 3 and references therein), and cavity-polariton effects and disorder effects (see, e.g., Ref. 4–11). Furthermore they are extensively used in applications such as vertical-cavity surface-emitting lasers (see, e.g., Ref. 12).

Besides their interesting linear optical properties, semiconductor microcavities have been found to yield insight into many nonlinear optical effects taking place in the semiconductor quantum well(s). Examples of such investigations include the nonlinear behavior of normal-mode coupling,[3] the observation of Rabi oscillations in microcavities[13] and nonlinear exciton correlation, biexcitonic, and polariton-scattering effects.[14–24]

Of course, semiconductors and semiconductor quantum wells exhibit challenging and interesting nonlinear optical effects even without being embedded in a microcavity (see, e.g., Refs. 25–29), but in the strong-coupling regime (i.e., near-zero detuning between the exciton and the cavity resonance in a high-Q cavity), the cavity changes strongly the linear and therefore also the nonlinear response of a quantum well. Furthermore, the new parametric degrees of freedom, e.g. detunings and finesse, introduced by the coupling to the cavity may refine our understanding of the physical nature of the quantum well's nonlinear response.

The purpose of this paper is to carry out a nonlinear optical response theory for semiconductor microcavities that is based on the fermionic electron-hole Hamiltonian, and that can be compared to experimental signals of microcavities. Specifically, we present a microscopic theory for the $\chi^{(3)}$ response of a quantum well microcavity around the heavy-hole exciton frequency. With the electron and hole masses as well as the background dielectric constant in the quantum well as basic input, it provides a detailed quantitative account of the effects of Pauli blocking, exciton scattering, bound coherent biexciton formation, and the cavity resonance.

While some investigations of microcavities are based on a full quantum-mechanical formulation (including a quantized light field), we adopt the semiclassical approach that has been used in most work in semiconductor optics: the radiation field is treated as classical while the charge carriers inside the quantum well are treated as a quantum many-body (fermion) system. The quantum part of the problem is formulated in the dynamics-controlled truncation (DCT) approach,[32] which has driven much recent progress in the microscopic understanding of weakly nonlinear response of semiconductors.[33–42]

In this paper we focus on the frequency regime around the heavy-hole exciton that allows us to restrict the $\chi^{(3)}$ DCT equations to the 1*s*-exciton subspace. While it is feasible with present-day computational resources to solve the full DCT equations with Maxwell's equations self-consistently, the tremendous simplification provided by the 1*s* truncation enables us to study features of exciton/polariton scattering in two dimensions in great detail, and to analyze the contributions of various effects in a much more transparent way.

Our theory agrees quantitatively with the recently published four-wave-mixing data by Gonokami and coworkers.[14,18] The detailed analysis given below reveals the signatures of both the bound biexciton and the exciton-exciton scattering (continuum) correlations. Furthermore, we will show that the full calculation of the scattering correlations is important: each of two common approximations, the

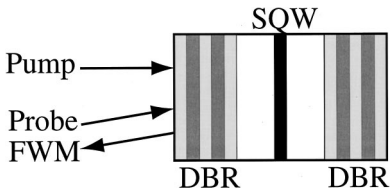

FIG. 1. Schematic drawing of the quantum-well microcavity. The reflected FWM signal is opposite in direction to the probe beam.

Markov and the second Born, results in clear discrepancies from the data. From general considerations in scattering theory, the second Born approximation is expected to fail in two dimensions, but it appears that a signal of its failure has not been experimentally identified in semiconductor nonlinear optics before.

In Sec. II we outline the basic theoretical approach and derive the expression for the $\chi^{(3)}$ susceptibility of a quantum well microcavity. In Sec. III we specialize to the four-wave-mixing (FWM) configuration and compare the theoretical results to the experimental data. We will discuss the relative contributions of various many-body effects. Some of the assumptions and approximations made in our theory will also be discussed and directions for future improvements and extensions indicated. In Sec. IV we summarize the main results.

II. MICROSCOPIC $\chi^{(3)}$ THEORY OF A QUANTUM WELL MICROCAVITY

In this section we derive the expression for the $\chi^{(3)}$ susceptibility of a quantum well microcavity. In Sec. II A, we define the model for the microcavity and develop the weak-field perturbation theory for its first and third order responses in terms of the quantum well's susceptibilities and the transfer matrices of the distributed Bragg reflectors. In Sec. II B, we derive the quantum well's $\chi^{(3)}$ susceptibility within the DCT (Ref. 32) framework.

A. Semiclassical treatment of a quantum well microcavity

A schematic diagram of our model for the microcavity is shown in Fig. 1. A quantum well (QW), flanked by spacer layers, is embedded between a pair of distributed Bragg reflectors (DBR). The semiclassical approach to light-matter coupling in semiconductor heterostructures has been explained in many works. In the dipole approximation, light propagation through the system is governed by Maxwell's equations with the induced polarization density as sources. We assume that the polarization density can be divided into a background dielectric part, which is local and linear in the electric field, and a resonant part which is in general nonlinear (see, e.g., Ref. 43). The background dielectric response is then expressed as a refractive index in the usual way. We will refer to the resonant part as the polarization density.

For simplicity, we develop the formalism only for the case where the propagation direction is normal to the plane of the QW and only the first subbands of the conduction and heavy-hole bands are resonantly excited.[44] The electric field and the polarization density are then parallel to the QW's plane, and they are assumed to be translationally invariant over this plane. This last assumption is valid if the radius of the cavity is at least several times larger than the wavelength of the light (see, e.g., Ref. 45). In each layer of the microcavity, the electric field satisfies the following wave equation in frequency space,

$$\left[n^2(z,\omega)\frac{\omega^2}{c^2}+\frac{\partial^2}{\partial z^2}\right]\mathbf{E}(z,\omega)=-4\pi\frac{\omega^2}{c^2}\mathbf{P}(z,\omega), \quad (2.1)$$

where the z axis is along the direction of the incident wave (Fig. 1). The refractive index n is taken to be a constant in each layer and over the frequency range we are interested in here. The resonant polarization density $\mathbf{P}$ is zero in the DBR's and the spacers. In the QW, it is calculated from the microscopic theory described in the next section. Equation (2.1) is supplemented by the conditions that $\mathbf{E}$ and $\partial\mathbf{E}/\partial z$ are continuous across each interface between two layers. Since only one subband is excited, the z dependence of $\mathbf{P}$ can be expressed by the band's confinement wave function $\xi(z)$ Ref. 44:

$$\mathbf{P}(z,\omega)=|\xi(z)|^2\mathbf{P}_{2D}(\omega), \quad (2.2)$$

where $\mathbf{P}_{2D}(\omega)$ is the in-plane polarization density. $\mathbf{P}_{2D}(\omega)$ is in general a functional of the average field inside the QW: $\mathbf{E}_Q(\omega)=\int dz|\xi(z)|^2\mathbf{E}(z,\omega)$ and may be expanded, within the rotating wave approximation, as follows:

$$\mathbf{P}_{2D}(\omega)=[\chi^{(1)}\mathbf{E}_Q](\omega)+[\chi^{(3)}\mathbf{E}_Q\mathbf{E}_Q\mathbf{E}_Q^*](\omega)+O(\mathbf{E}_Q^5), \quad (2.3)$$

where $\chi^{(1)}$ and $\chi^{(3)}$ are the linear and third-order susceptibilities of the two-dimensional (2D) model of the QW, respectively, and we have used the notation

$$[\chi^{(1)}\mathbf{E}_Q]_i(\omega)=\sum_j \chi_{ij}^{(1)}(\omega)E_{Qj}(\omega)$$

$$[\chi^{(3)}\mathbf{E}_Q\mathbf{E}_Q\mathbf{E}_Q^*]_i(\omega)=\frac{1}{(2\pi)^2}\sum_{jkl}\int d\omega_1 d\omega_2 d\omega_3\,\delta(\omega_1+\omega_2-\omega_3-\omega)\chi_{ijkl}^{(3)}(\omega_1,\omega_2,\omega_3)\cdot E_{Qj}(\omega_1)\times E_{Qk}(\omega_2)E_{Ql}^*(\omega_3) \quad (2.4)$$

with i,j,k,l being the spatial vector/tensor component indices. Substituting the expressions (2.2) and (2.3) for $\mathbf{P}(z,\omega)$ in Eq. (2.1), we obtain a nonlinear integro-differential equation for the electric field inside the QW. If the incident field is weak, and the dephasing times are not too long, the field inside the QW may be expanded perturbatively in the incident field (or its peak amplitude): $\mathbf{E}(z,\omega)=\mathbf{E}^{(1)}(z,\omega)+\mathbf{E}^{(3)}(z,\omega)+\cdots$ for z inside the QW. Then, expanding Eq. (2.1) and collecting terms of the same order, we obtain a sequence of equations, the first two of which are

$$\left[n_b^2\frac{\omega^2}{c^2}+\frac{\partial^2}{\partial z^2}\right]\mathbf{E}^{(1)}(z,\omega)=-4\pi\frac{\omega^2}{c^2}|\xi(z)|^2[\chi^{(1)}\mathbf{E}_Q^{(1)}](\omega), \tag{2.5}$$

$$\left[n_b^2\frac{\omega^2}{c^2}+\frac{\partial^2}{\partial z^2}\right]\mathbf{E}^{(3)}(z,\omega)=-4\pi\frac{\omega^2}{c^2}|\xi(z)|^2\{[\chi^{(1)}\mathbf{E}_Q^{(3)}](\omega)+[\chi^{(3)}\mathbf{E}_Q^{(1)}\mathbf{E}_Q^{(1)}\mathbf{E}_Q^{(1)*}](\omega)\}, \tag{2.6}$$

where n_b is the background refractive index of the QW material. The iterative method of solution of the above equations, with the QW susceptibilities $\chi^{(1)}$ and $\chi^{(3)}$ as material input, and the transfer matrices relating the electric field outside the cavity to that inside the QW, are given in Appendix A. The relevant result is that the third-order reflected ($\mathbf{E}_r^{(3)}$) and transmitted ($\mathbf{E}_t^{(3)}$) fields outside the cavity are related to the incident field ($\mathbf{E}_0$) as

$$\mathbf{E}_{r/t}^{(3)}(z_t/z_b,\omega)=C_{r/t}(\omega)[\chi^{(3)}\mathbf{E}_Q^{(1)}\mathbf{E}_Q^{(1)}\mathbf{E}_Q^{(1)*}](\omega), \tag{2.7}$$

$$\mathbf{E}_Q^{(1)}(\omega)=C^{(1)}(\omega)\mathbf{E}_0(z_t,\omega), \tag{2.8}$$

where C_r, C_t, and $C^{(1)}$ are the cavity enhancement factors given in Appendix A (compare Ref. 46), and z_t and z_b are the positions of the cavity's end points on the left (air) and right (substrate) sides, respectively. For the applications considered here, $\chi^{(1)}$ is dominated by one exciton (heavy-hole) resonance. The microscopic theory for $\chi^{(3)}$ in this energy range, accounting for the interactions among the excitons, is treated in the next section.

B. Microscopic theory of the single-quantum-well $\chi^{(3)}$ susceptibility

We work within the DCT scheme,[32] which is a perturbative (in the applied field) density-matrix formalism designed to efficiently treat Coulomb correlations among carriers in coherent optical processes. Under the assumptions that (i) the initial state is the ground state, and (ii) the Coulomb interaction does not induce interband transitions, DCT gives a recipe to derive in principle exact, closed equations of motion for all contributing correlation functions up to any given order in the applied field. Although an approximate microscopic treatment of phonon dephasing is possible,[47,48] it is a much more elaborate undertaking that is still being developed. Instead, we will adopt the common practice of lumping dephasings from all sources other than carrier-carrier scattering into a set of phenomenological constants.

Our model for the electronic dynamics around the lowest absorption band edge in the QW consists of two parabolic bands in two dimensions. The Hamiltonian is

$$\hat{H}=\hat{H}_1+\hat{H}_2+\hat{H}_{field} \tag{2.9}$$

$$\hat{H}_1=\sum_{\mathbf{k}e}\left[\frac{\hbar^2k^2}{2m_e}+E_g\right]a_e^\dagger(\mathbf{k})a_e(\mathbf{k})+\sum_{\mathbf{k}h}\frac{\hbar^2k^2}{2m_h}a_h^\dagger(\mathbf{k})a_h(\mathbf{k})$$

$$\hat{H}_2=\frac{1}{2A}\sum_{\mathbf{q}\neq0,\mathbf{k}\mathbf{k}'}V(\mathbf{q})\cdot\Bigg[\sum_{ee'}a_e^\dagger(\mathbf{k}+\mathbf{q})a_{e'}^\dagger(\mathbf{k}'-\mathbf{q})\times a_{e'}(\mathbf{k}')a_e(\mathbf{k})+\sum_{hh'}a_h^\dagger(\mathbf{k}+\mathbf{q})a_{h'}^\dagger(\mathbf{k}'-\mathbf{q})a_{h'}(\mathbf{k}')a_h(\mathbf{k})-\sum_{eh}(a_e^\dagger(\mathbf{k}+\mathbf{q})a_h^\dagger(\mathbf{k}'-\mathbf{q})a_h(\mathbf{k}')a_e(\mathbf{k})+a_h^\dagger(\mathbf{k}+\mathbf{q})a_e^\dagger(\mathbf{k}'-\mathbf{q})a_e(\mathbf{k}')a_h(\mathbf{k}))\Bigg]$$

$$\hat{H}_{field}=\sum_{eh\mathbf{k}}[\mathbf{d}_{eh}\cdot\mathbf{E}(t)a_e^\dagger(\mathbf{k})a_h^\dagger(-\mathbf{k})+\mathbf{d}_{he}\cdot\mathbf{E}(t)a_h(-\mathbf{k})a_e(\mathbf{k})],$$

where $m_e(m_h)$ is the electron (hole) mass, E_g is the band gap, $\mathbf{d}_{eh}\equiv q_e\langle e|\mathbf{r}|v\rangle$ is the transition dipole matrix element, $V(\mathbf{q})=2\pi q_e^2/\epsilon_b|\mathbf{q}|$, q_e is the magnitude of the electron's charge, ϵ_b is the background dielectric constant of the QW material, and A is the area of the normalization box. The characteristic length and energy scales of this system are, respectively, the exciton Bohr radius $a_0\equiv\hbar^2\epsilon_b/q_e^2m_r$, m_r being the electron-hole reduced mass, and the 2D exciton Rydberg $E_b\equiv2\hbar^2/m_ra_0^2$. The subscripts e,h,e',h' represent all quantum numbers other than the momentum of the single particle or hole orbitals in the respective bands. As can be seen, only the part of the Coulomb interaction that does not cause an interband transition is retained in the model. The remainder, which is responsible for Auger transitions and longitudinal-transverse splitting of the exciton modes, is not important here. As mentioned above, this approximation makes the tremendous simplification of the many-body problem in the DCT formalism possible. The ground state of the system is the electron-hole vacuum, which is assumed to be stable against electron-hole creation by virtue of a large enough E_g.

Within the $\chi^{(3)}$ regime, DCT expresses the carrier dynamics by a coupled pair of equations for the interband polarization and the two-electron–two-hole (biexcitonic) correlation. We follow here Ref. 29 (see also Refs. 35 and 49) as far as the expansion of these equations in the exciton eigenfunction basis is concerned. As explained above, we restrict the equations to the $1s$ heavy-hole exciton subspace. We denote by $p_\pm(t)$ the interband polarization arising from the optical transition from the ground state to this subspace:

$$p_\pm(t)=\sum_{\mathbf{k}eh}\phi^*(\mathbf{k})\langle a_h(-\mathbf{k})a_e(\mathbf{k})\rangle\delta_{j_e+j_h,\pm1}, \tag{2.10}$$

where $j_e=\pm1/2$ and $j_h=\pm3/2$ are the z components of the ''spin'' angular momenta of the electron orbital e and the hole orbital h, respectively, and $\phi(\mathbf{k})=\sqrt{2\pi}a_0/[1+(a_0k/2)^2]^{3/2}$ is the normalized $1s$ heavy-hole exciton wave function (assumed to be spin-independent). We use the subscripts $\pm$ to distinguish the two optical transitions (excitons)

coupled to right- and left-handed circularly polarized light, respectively. In the DCT scheme, the interband polarization is expanded in the applied field: $p_{\pm}=p_{\pm}^{(1)}+p_{\pm}^{(3)}+\ldots$, the order being indicated by the superscript. Solving the DCT equations iteratively, starting from the linear order, one obtains a compact equation for the third-order circularly polarized interband polarization (see Refs. 29 and 49 for details):

$$\begin{aligned} i\hbar\frac{d}{dt}p_{\pm}^{(3)}(t) &= [\varepsilon(\mathbf{0})-i\gamma_2]p_{\pm}^{(3)}(t)-2\Omega_{\pm}(t)A^{PSF}p_{\pm}^{(1)}(t)p_{\pm}^{(1)*}(t) \\ &+V^{HF}p_{\pm}^{(1)}(t)p_{\pm}^{(1)}(t)p_{\pm}^{(1)*}(t)+2p_{\pm}^{(1)*}(t) \\ &\times\int_{-\infty}^{\infty}dt'\tilde{G}^{+}(t-t')p_{\pm}^{(1)}(t')p_{\pm}^{(1)}(t') \\ &+p_{\mp}^{(1)*}(t)\int_{-\infty}^{\infty}dt'[\tilde{G}^{+}(t-t') \\ &+\tilde{G}^{-}(t-t')]p_{\mp}^{(1)}(t')p_{\pm}^{(1)}(t'), \end{aligned} \tag{2.11}$$

where $\Omega_{\pm}(t)$ is the Rabi frequency (times $\hbar$), $\varepsilon(\mathbf{q})$ is the energy of an exciton with center-of-mass momentum $\mathbf{q}$, and γ_2 is a phenomenological dephasing constant of the exciton resonance. The terms proportional to A^{PSF}, V^{HF}, and $\tilde{G}^{\pm}(t-t')$ are, respectively, the contributions from phase-space filling, the exciton mean field, and the retarded correlations due to higher-order (beyond first Born) scatterings between two excitons and/or the bound biexciton resonance. In terms of the heavy-hole $1s$ wave function $\phi(\mathbf{k})$, the constants A^{PSF} and V^{HF} are given by

$$A^{PSF}=\sum_{\mathbf{k}}|\phi(\mathbf{k})|^2\phi(\mathbf{k})=\frac{4\sqrt{2\pi}}{7}a_0 \tag{2.12}$$

$$\begin{aligned} V^{HF}&=2\sum_{\mathbf{k}\mathbf{k}'}V(\mathbf{k}-\mathbf{k}')|\phi(\mathbf{k})|^2\phi(\mathbf{k}')[\phi^*(\mathbf{k})-\phi^*(\mathbf{k}')] \\ &\approx 1.514a_0^2E_b. \end{aligned} \tag{2.13}$$

The superscript $\lambda=+/-$ on the retarded correlation kernel $\tilde{G}^{\lambda}(t-t')$ labels the total electron-spin state of the two colliding excitons: $+(-)$ for triplet (singlet). This classification takes advantage of the block diagonality of the effective two-exciton Hamiltonian in the total electron-spin channels. In terms of this Hamiltonian $H^{xx(\lambda)}$ (the superscript ''xx'' stands for ''exciton-exciton''), the retarded correlation kernel is given by

$$\begin{aligned} \tilde{G}^{\lambda}(t-t')=\frac{1}{2i\hbar}\theta(t-t')\sum_{\mathbf{q}\mathbf{q}'\mathbf{q}''}W_{\mathbf{q},\mathbf{0}}^{xx(\lambda)*}[\exp\{-(i/\hbar)(H^{xx(\lambda)} \\ -i\gamma_b I)(t-t')\}]_{\mathbf{q},\mathbf{q}''}[I-\lambda S]^{-1}_{\mathbf{q}'',\mathbf{q}'}W_{\mathbf{q}',\mathbf{0}}^{xx(\lambda)} \end{aligned} \tag{2.14}$$

with

$$H_{\mathbf{q},\mathbf{q}'}^{xx(\lambda)}=2\varepsilon(\mathbf{q})\delta_{\mathbf{q}\mathbf{q}'}+\sum_{\mathbf{q}''}[I-\lambda S]^{-1}_{\mathbf{q},\mathbf{q}''}W_{\mathbf{q}'',\mathbf{q}'}^{xx(\lambda)}. \tag{2.15}$$

Here, $W_{\mathbf{q},\mathbf{q}'}^{xx(\lambda)}$ is the Coulomb matrix element including exchange between an initial exciton state with relative momentum $\mathbf{q}'$ and the final state $\mathbf{q}$, and $S_{\mathbf{q},\mathbf{q}'}$ is a matrix of overlap integrals between the nonorthonormal antisymmetrized two-exciton basis states. The expressions of these two matrices are given in Appendix B. We have included in Eq. (2.14) another phenomenological dephasing constant γ_b for the two-exciton states.

The 2D polarization density in Sec. II A is given in terms of the interband polarization. Denoting $P_{2D}^{(1)}\equiv[\chi^{(1)}\mathbf{E}_Q^{(1)}]$ and $P_{2D}^{(3)}\equiv[\chi^{(3)}\mathbf{E}_Q^{(1)}\mathbf{E}_Q^{(1)}\mathbf{E}_Q^{(1)*}]$, we have

$$P_{2D\pm}^{(n)}=-d_{\pm}^{0}p_{\pm}^{(n)},\quad n=1,3 \tag{2.16}$$

where $d_{\pm}^{0}\equiv\tilde{\phi}(\mathbf{0})q_e\langle r_{\pm}\rangle^*$, $\tilde{\phi}(\mathbf{0})$ is the configuration space $1s$ exciton wavefunction at $\mathbf{r}=\mathbf{0}$, and $\langle r_{\pm}\rangle\equiv\langle c|(x\pm iy)/\sqrt{2}|v\rangle$ is the transition dipole matrix element. Fourier transforming Eq. (2.11) to frequency space, and noting Eq. (2.16), yields the third-order susceptibility defined in Eq. (2.3). Within the heavy-hole $1s$ model space, $\chi_{ij}^{(1)}$ (with $i,j=\{+,-\}$) is a scalar: $\chi_{ij}^{(1)}=\delta_{ij}\chi^{(1)}$, and, as can be seen from Eq. (2.11), $\chi_{ijkl}^{(3)}$ has only two independent nonvanishing components:

$$\begin{aligned} \chi_{ijkl}^{(3)}(\omega_1,\omega_2,\omega_3)=\frac{1}{2}[\delta_{ij}\delta_{kl}\chi_{ik}^{(3)}(\omega_1,\omega_2,\omega_3) \\ +\delta_{ik}\delta_{jl}\chi_{ij}^{(3)}(\omega_2,\omega_1,\omega_3)], \end{aligned} \tag{2.17}$$

$i,j,k,l=+/-$, and $\chi_{++}^{(3)}=\chi_{--}^{(3)}$, $\chi_{+-}^{(3)}=\chi_{-+}^{(3)}$. Explicitly,

$$\begin{aligned} \chi_{ij}^{(3)}(\omega_1,\omega_2,\omega_3) &= -\frac{\chi^{(1)}(\omega_1)\chi^{(1)}(\omega_2)\chi^{(1)*}(\omega_3)\chi^{(1)}(\omega_1+\omega_2-\omega_3)}{q_e^4|\langle r_+\rangle|^4|\tilde{\phi}(\mathbf{0})|^4} \\ &\times[\delta_{ij}G^{PSF}(\omega_1,\omega_2)+T^{ij}(\omega_1+\omega_2)], \end{aligned} \tag{2.18}$$

where

$$T^{++}(\Omega)=V^{HF}+2G^{+}(\Omega),\quad T^{+-}(\Omega)=G^{+}(\Omega)+G^{-}(\Omega). \tag{2.19}$$

Here $G(\Omega)$ is the Fourier transform of $\tilde{G}(t)$,

$$\begin{aligned} G^{(\lambda)}(\Omega)=\frac{1}{2}\sum_{\mathbf{q}\mathbf{q}'}W_{\mathbf{q},\mathbf{0}}^{xx(\lambda)*} \\ \times\left[\frac{1}{\hbar\Omega-H^{xx(\lambda)}+i\gamma_b}(1-\lambda S)^{-1}\right]_{\mathbf{q},\mathbf{q}'}W_{\mathbf{q}',\mathbf{0}}^{xx(\lambda)}, \end{aligned} \tag{2.20}$$

the phase space filling contribution is

$$\begin{aligned} G^{PSF}(\omega_1,\omega_2)=A^{PSF}q_e^2|\langle r_+\rangle|^2\tilde{\phi}^*(\mathbf{0}) \\ \times\left[\frac{1}{\chi^{(1)}(\omega_1)}+\frac{1}{\chi^{(1)}(\omega_2)}\right]. \end{aligned} \tag{2.21}$$

With all effects extraneous to our Hamiltonian embodied in the dephasing parameter γ_2, the linear polarization is given within our model by a Lorentzian

$$\chi^{(1)}(\omega) = -\frac{q_e^2 |\langle r_+ \rangle|^2 |\tilde{\phi}(\mathbf{0})|^2}{\hbar\omega - \varepsilon(\mathbf{0}) + i\gamma_2}, \quad \text{for } \omega > 0. \quad (2.22)$$

In this case, the bracketed sum of two reciprocal $\chi^{(1)}$'s in Eq. (2.22) reduces to a function depending only on the sum of the two excitons' energies: $2/\chi^{(1)}(\Omega/2)$, $\Omega = \omega_1 + \omega_2$, which is the form we use in this paper. In a more exact treatment including, for example, phonon dynamics, the exciton line shape $[\mathrm{Im}(\chi^{(1)})]$ exhibits the so-called Urbach tail and is different from a Lorentzian, in which case G^{PSF} in Eq. (2.21) is a function of ω_1 and ω_2 separately.

Equation (2.18) has a very simple structure. It gives the third-order susceptibility as a product of $\chi^{(1)}$'s (which carry single-exciton propagation effects) and two-exciton Pauli-blocking and interaction terms. We have calculated G^{λ} by numerically diagonalizing the Hamiltonian $H^{xx(\lambda)}$ and constructing the Green's operator $(\hbar\Omega - H^{xx(\lambda)} + i\gamma_b)^{-1}$ as an eigenfunction expansion. Note that since $W^{xx(\lambda)}$ has an electron (or hole)-exchange term, optically inactive exciton states are also included in the eigenfunction basis here. A complication arises here regarding the overlap matrix S (also truncated to the $1s$ subspace): it has one eigenvalue close to 1, leading to a spurious peak structure in the triplet-state correlation kernel $G^{(+)}(\Omega)$.[49] Although this spurious peak emerges only at an energy above the spectral range (-5 meV $< \hbar\omega - \varepsilon(\mathbf{0}) <$ 5 meV) under consideration in this paper, it nevertheless indicates that the presence of the matrix $(1 - S)^{-1}$ might amplify the shortcomings of the 1s approximation, and a quantitative analysis might be better with S being neglected. A detailed discussion of this issue will be given in Ref. 49. All the results shown in this paper, unless it is stated otherwise, are calculated with S set to zero. We note that the issue of whether to include S is not critical to the particular application of our theory examined in this paper. The conclusions reached below about various approximations are valid with or without the overlap matrix. In the next section, the predictions with S included are shown (cf. Fig. 13) to also fit the experiment quite well.

Figures 2 and 3 show T^{ij} and its components V^{HF} and $G^{\pm}(\Omega)$, together with $G^{PSF}(\Omega)$ for GaAs parameters: $m_e = 0.067m_0, m_h = 0.1m_0$, where m_0 is the electron mass in free space, $\epsilon_b = 13$, and $\gamma_b = 1.5$ meV. $G^{-}(\Omega)$ has been further broken down into contributions from the bound biexciton and the two-exciton continuum states.

If $W^{xx(\lambda)}$ were Hermitian, and if we take $S = 0$, the quantity $T^{ij}(\Omega)$ defined in Eq. (2.20) has the form of the off-energy-shell forward scattering (or T-) matrix element for two (virtual) particles at zero momentum and total energy Ω (compare Ref. 50). The truncation to the $1s$ subspace and the inclusion of exchange result in a non-Hermitian $W^{xx(\lambda)}$ in our case, but we will see, in spite of this non-Hermiticity, general scattering theory (e.g., Ref. 51) is still quantitatively useful in understanding the behavior of our numerical results. For example, it is known that, in *two* dimensions, the zero-momentum off-energy-shell T-matrix for two colliding particles behaves asymptotically at low energies as[52] $T(z) \approx -2\pi\hbar^2/M_r 1/\ln[(-z)/\varepsilon_c]$, where z is the (complex) energy in the center-of-mass frame and M_r is the reduced mass. This asymptotic behavior is valid for any generic Hermitian, short-range, even nonlocal, interaction, and it holds for $|z| \ll \varepsilon_c$, where ε_c is an energy scale that depends on the specific interaction for each problem. For an equilibrium 2D quantum gas in the dilute limit, the effects of the interaction on the system's thermodynamic behavior are summarized in ε_c [Ref. 53]. In terms of excitonic terminology and units, this asymptotic formula reads:

$$T(\hbar\Omega + i\gamma_b) \approx -\frac{2\pi\alpha(1-\alpha)}{\ln\{-[\hbar\Omega - 2\varepsilon(\mathbf{0}) + i\gamma_b]/\varepsilon_c\}} a_0^2 E_b . \quad (2.23)$$

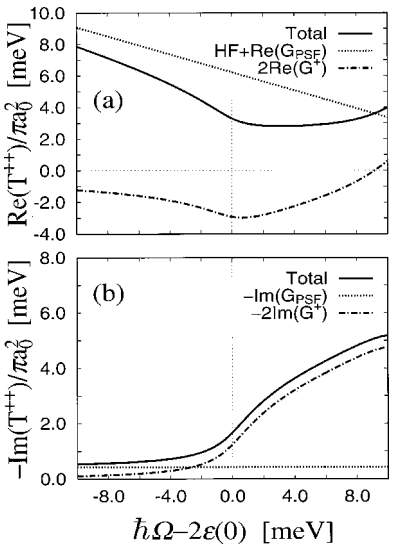

FIG. 2. Exciton-exciton (off-energy-shell) forward-scattering amplitude at zero momentum in the co-circularly polarization channel and its constituent components.

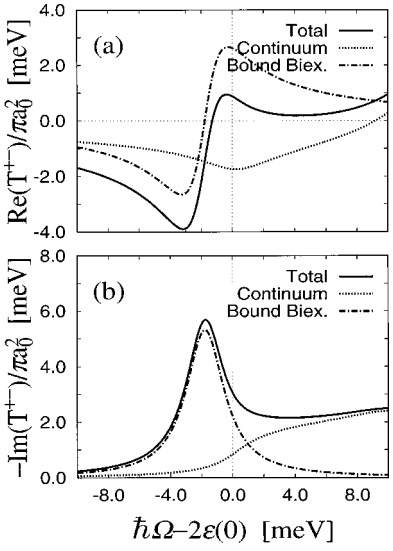

FIG. 3. Exciton-exciton (off-energy-shell) forward-scattering amplitude at zero momentum in the counter-circularly polarization channel and its constituent components.

where $\alpha = m_h/(m_e+m_h)$, $2\varepsilon(\mathbf{0})$ is the continuum edge. In Figs. 2 and 3, T^{ij} shows only a hint of a nonsmooth logarithmic behavior around the continuum edge, but we have found in more detailed numerical studies[49,54] that, for $\gamma_b \searrow 0$ and the range $|\hbar\Omega - 2\varepsilon(\mathbf{0})| < 0.01E_b$, our computed T^{ij} obeys almost exactly the 1/ln behavior of Eq. (2.23) [with $\varepsilon_c \approx 0.6E_b$ and a numerical constant in the numerator ≈ 1.4 times that in Eq. (2.23) in the $(++)$ channel, for example]. Equation (2.23) implies that, in the $(++)$ configuration for instance, there is exact cancellation between the Hartree-Fock and the correlation terms at $\hbar\Omega - 2\varepsilon(\mathbf{0}) = \gamma_b = 0$, which is related to the sum rule of Ref. 41. The 1/ln function however varies rapidly near the origin, and our numerical results (Fig. 2) show that T^{++} is no longer small only a short distance away from the continuum edge and/or for a moderate value of γ_b, 1 meV say. This tendency for the correlation term to partially cancel the Hartree-Fock term was also noted in Refs. 37,42.

Again, if $W^{xx(\lambda)}$ were Hermitian, $-\mathrm{Im}\, G^{\lambda}(\Omega)$ would be non-negative and would yield the rate of scattering of two virtual excitons of total energy $\hbar\Omega$ and zero momentum into real excitons of the same energy $\hbar\Omega$ and momenta given by the dispersion relation $\hbar|\mathbf{q}| = \sqrt{[\hbar\Omega - 2\varepsilon(\mathbf{0})](m_e+m_h)}$. Furthermore, if $\mathrm{Im}\, G^{\lambda}(\Omega)$ goes to zero sufficiently fast at $\Omega \to \infty$, then G^{λ} is analytic in the upper half of the complex energy plane. Then for $\gamma_b \searrow 0$, the real and imaginary parts of $G^{(\lambda)}$ would obey a Kramers-Kronig relation, according to which $\mathrm{Re}G^{\lambda}$ would be negative at large negative energies, cross zero (at least once) inside the support of $\mathrm{Im}G^{\lambda}$ (i.e., the spectrum of the two-exciton Hamiltonian), and is positive for large positive energies. Figures 2 and 3 show that, even with our non-Hermitian $W^{xx(\lambda)}$, G^{λ} displays these behaviors quite well within the relevant energy range $(-10\ \mathrm{meV} < \hbar\Omega - 2\varepsilon(\mathbf{0}) < 10\ \mathrm{meV})$ in this paper. At higher energies, our calculated $-\mathrm{Im}\, G^{\lambda}(\Omega)$ actually violates non-negativity slightly over a very short energy span, which disallows an extension to these energies of the present model without modifications. These issues will be discussed in more detail in Ref. 49.

Our numerical results thus support the interpretation, with the caveats discussed above, of $T^{ij}(\Omega)$ as the forward-scattering off-energy-shell T matrix for two virtual excitons (Fig. 4). As is well known, the T-matrix plays a dominant role in the statistical mechanical properties of dilute nonideal quantum gases.[55] The microcavity FWM experiment to be analyzed in the next section may thus be considered a probe of this important quantity for the interacting exciton system. The identification of $-\mathrm{Im}\, G^{\lambda}(\Omega)$ with the rate of virtual-to-real exciton scattering also gives a microscopic underpinning[56–58] of excitation-induced dephasing as usually used in phenomenological models.[59–66]. However, the physical process underlying excitation-induced dephasing depends strongly on the excitation conditions, so that processes different from those considered here may be relevant in other experimental settings.

In $\chi^{(3)}$ treatments, the second-Born approximation, corresponding to keeping only the first term (kinetic energy) in Eq. (2.15), is often used to estimate the continuum contributions to the exciton-exciton correlation (e.g., Ref. 67). While this approximation may be adequate in 3D, it is quantitatively unsatisfactory in 2D because, for vanishing γ_b, Im G^{+} and the continuum part of $\mathrm{Im}\, G^{-}$ would develop a disconti nuity at $2\varepsilon(\mathbf{0})$ [see Eq. (2.20)] while their real parts would develop logarithmic divergences. A finite γ_b would temper these singular behaviors, but Fig. 5 shows that, even at the relatively large $\gamma_b = 1.5$ meV, the residual effect of the singularity is still considerable. In the next section, we will show that the experimental results that we analyze are sufficiently sensitive to distinguish between the predictions of the exact-scattering theory and its second-Born approximation.

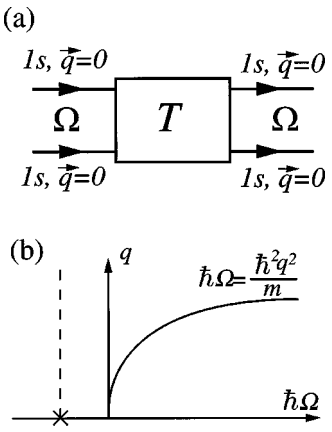

FIG. 4. (a) Schematic of the exciton T matrix measured in coherent $\chi^{(3)}$ experiments. The momenta of the initial and final states are zero, but the energy is given by the sum of the frequencies of the light fields that create the excitons. (b) Schematic of the domain of the excitonic T matrix. The cross and dashed line indicate the position of the biexciton pole.

The Markovian limit is another approximation sometimes used to simplify computations of Coulomb correlations in the continuum (e.g., Ref. 67). In the present context, we define this limit to be the short memory-time limit of the continuum part of the retarded exciton-exciton correlation kernel $\tilde{G}^{\pm}(t-t')$ in Eq. (2.11). More precisely, it is the assumption that the continuum part of $\tilde{G}^{\pm}(t-t')$ decays on a time scale fast compared to the variation of $e^{i\varepsilon(\mathbf{0})t}p_{\pm}^{(1)}(t)$. If this is the case, one may to a good approximation replace t', the time argument of $p_{\pm}^{(1)}$ inside the integral in Eq. (2.12), by t and take $p_{\pm}^{(1)}$ outside the integral. In frequency space, this amounts to approximating the T matrix elements by their

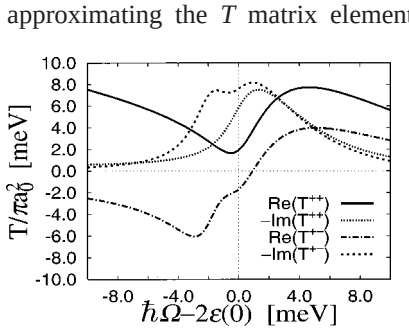

FIG. 5. Exciton-exciton T-matrix in the second-Born approximation.

respective values at $\Omega = 2\varepsilon(\mathbf{0})$. As noted above, the T-matrix at this energy vanishes in the small-damping limit $\gamma_b \searrow 0$, thus guaranteeing the Markov approximation to be poor in this limit. For $\gamma_b = 1.5$ meV, Figs. 3 and 2 shows that taking this approximation still reduces quite substantially the contribution of ImG, the scattering rate of virtual excitons to real excitons, in the continuum. We will also discuss the effect of this approximation on the FWM signals in the next section.

III. COMPARISON WITH EXPERIMENT

In this section we specialize to the degenerate four-wave-mixing (DFWM) configuration and compare our calculated signals with the experimental results reported in Refs. 14,18. In the experiment, a 120-Å GaAs quantum well with a pair of 670-Å AlAs spacers were used. The right DBR was composed of 22 pairs of GaAs/AlAs layers and the left DBR 14.5 pairs. The exciton resonance energy $\varepsilon(\mathbf{0})$ was fixed while the cavity resonance frequency ω_c could be varied. Two long-pulsed beams of the same central frequency were incident on the left surface, the pump (p) beam being exactly normal to the surface and the probe (t) beam slightly angled (Fig. 1). The intensity of the reflected FWM signal, which is opposite in direction to the incident probe beam, was measured as a function of the beam frequency. This measurement was performed for various values of the cavity-exciton detuning $\Delta \equiv \hbar\omega_c - \varepsilon(\mathbf{0})$ and various polarization combinations of pump (σ_p), probe (σ_t), and signal (σ_s) beams.

We show in Fig. 6 the reflected FWM signal intensities for zero exciton-cavity detuning as calculated in our theory and compare them to the measurements in Refs. 14,18. The results are displayed as functions of the beam frequency for four polarization combinations, which are designated in the order $(\sigma_p, \sigma_t, \sigma_s)$, $\sigma = x, y, +$, or $-$. Also shown is the linear reflectivity, from which we extract our model $\chi^{(1)}$ parameters: $\varepsilon(\mathbf{0}) = 1.552$ eV, $\gamma_2 = 0.75$ meV, and $|\tilde{\phi}(\mathbf{0})\langle r_+ \rangle| = 0.035$. The other parameter values for the electron-hole hamiltonian Eq. (2.9) have been given at the end of Sec. II B. The phenomenological damping constant γ_b in Eq. (2.21) represents the dephasing and decay of the correlated, coherent two-exciton systems and is, for homogeneously broadened excitons, commonly attributed to radiative decay and phonon scattering.[68] Its value is set to $2\gamma_2$ here, based on simple considerations on phonon dephasing that have received some experimental support recently.[68] While this estimate may turn out not to be perfectly accurate, we note that the predicted FWM signals here are not very sensitive to variations of γ_b up to several tens of percent. The refractive indices are set to 3.59 for GaAs and 2.98 for AlAs. A small imaginary part, 0.0015, is added to each refractive index to fit the experimental width of the cavity resonance.

The linear reflectivity spectrum shows the characteristic normal-mode splitting. The FWM signals are dominated by peaks at or very close to the two polariton energies. The signals have been normalized by matching the theoretical and experimental peak heights at the lower polariton peak in the (x,y,y) channel. The relative strengths of the signal peaks, and their polarization dependence, are, as explained in detail below, manifestations of the microscopic many-exciton dynamics. One notes here that there is good quantitative agreement between our theory and the experiment.

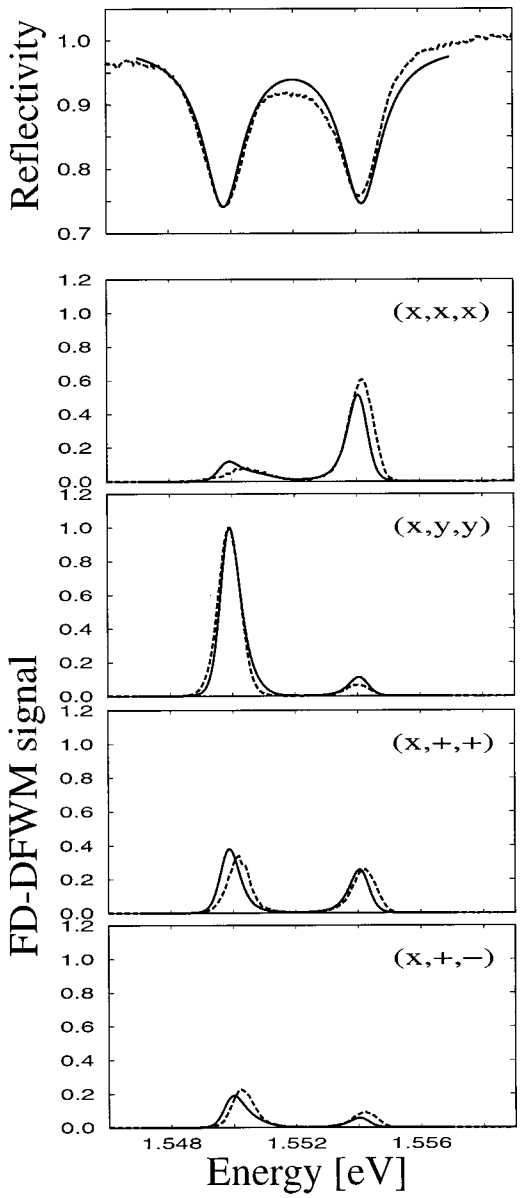

FIG. 6. Comparison between theory (solid line) and experiment (dashed line) for frequency-domain degenerate FWM signals (FD-DFWM) from a quantum-well microcavity at zero detuning between the lowest QW exciton resonance and the cavity resonance, both at 1.552 eV. The polarizations in each panel are designated in the order (pump, probe, signal). The linear reflection spectrum is shown on top.

To better interpret the data, we first give a detailed analysis of the spectral features of the FWM signals within our theory. Each of the three electric fields in Eq. (2.6) is a sum of the pump and the probe fields: $\mathbf{E}_Q^{(1)} = \mathbf{E}_Q^{(1)p} + \mathbf{E}_Q^{(1)t}$. The slightly oblique positioning of the probe beam allowed the experimentalist to selectively measure the FWM signals, which comes from the field combination $\mathbf{E}_Q^{(1)p}(\omega_1)\mathbf{E}_Q^{(1)p}(\omega_2)\mathbf{E}_Q^{(1)t*}(\omega_3)$. In our theory that treats only normally incident beams, retaining only this combination as

a source of the $\chi^{(3)}$ interband polarization should give an adequate approximation to the signals in the slightly angled configuration. We assume continuous-wave input beams: $\mathbf{E}_0^p(\omega_1)=2\pi\boldsymbol{\mathcal{E}}^p\delta(\omega_1-\omega)$ etc., where ω denotes the beam frequency, in which case, only the diagonal ($\omega_1=\omega_2=\omega_3=\omega$) part of the third order susceptibility Eq. (2.19) contributes to the responses:

$$\chi^{(3)}_{ij}(\omega,\omega,\omega)=-\frac{|\chi^{(1)}(\omega)|^2[\chi^{(1)}(\omega)]^2}{q_e^4|\langle r_+\rangle|^4|\tilde{\phi}(\mathbf{0})|^4}[\,\delta_{ij}G^{PSF}(2\omega)+T^{ij}(2\omega)],\quad i,j=+/-. \tag{3.1}$$

Under these conditions, the FWM signal is also a monochromatic beam of frequency ω. Its time-averaged flux intensity for the polarization combinations in the experiment can be written, from Eqs. (2.4), (2.7), (2.8), and (3.1), as

$$I^{(3)}_{r(\sigma_p,\sigma_t,\sigma_s)}(\omega,\Delta)=D(\omega,\Delta)|\tilde{\mathcal{T}}_{(\sigma_p,\sigma_t,\sigma_s)}(\omega)|^2\,|\mathcal{E}^p|^4\,|\mathcal{E}^t|^2, \tag{3.2}$$

where the factor

$$D(\omega,\Delta)=\frac{c}{8\pi}|C_r(\omega,\Delta)|^2\,|C^{(1)}(\omega,\Delta)|^6\frac{|\chi^{(1)}(\omega)|^8}{|q_e\langle r_+\rangle\tilde{\phi}(\mathbf{0})|^8} \tag{3.3}$$

carries the dependence on the cavity and the single-exciton propagation, and $\tilde{\mathcal{T}}_{(\sigma_p,\sigma_t,\sigma_s)}(\omega)$ contains the exciton interaction and Pauli-blocking effects

$$\begin{aligned}
\tilde{\mathcal{T}}_{(x,x,x)}(\omega)&=G^{PSF}(2\omega)+T^{++}(2\omega)+T^{+-}(2\omega),\\
\tilde{\mathcal{T}}_{(x,y,y)}(\omega)&=-G^{PSF}(2\omega)-T^{++}(2\omega)+T^{+-}(2\omega),\\
\tilde{\mathcal{T}}_{(x,+,+)}(\omega)&=G^{PSF}(2\omega)+T^{++}(2\omega),\\
\tilde{\mathcal{T}}_{(x,+,-)}(\omega)&=T^{+-}(2\omega).
\end{aligned} \tag{3.4}$$

For the purpose of understanding excitonic dynamics, the advantage of writing the signal in this way is clear: the dependences on polarization combination and cavity-exciton detuning Δ, reside separately in $\tilde{\mathcal{T}}_{(\sigma_p,\sigma_t,\sigma_s)}(\omega)$ and $D(\omega,\Delta)$ respectively. $D(\omega,\Delta)$ shows two peaks at the polariton energies that shift when the detuning Δ is varied. Hence the ω dependence of $|\tilde{\mathcal{T}}_{(\sigma_p,\sigma_t,\sigma_s)}(\omega)|$ predicts the variations of the signal peak height with Δ. On the other hand, the relative contributions of the various many-body ingredients to $|\tilde{\mathcal{T}}_{(\sigma_p,\sigma_t,\sigma_s)}(\omega)|$, and the reinforcements and cancellations among them, governs the polarization dependence of the signal at a fixed detuning.

In Fig. 7 we plot the functions $|\tilde{\mathcal{T}}_{(\sigma_p,\sigma_t,\sigma_s)}(\omega)|^2$. No comment is needed on the behavior of $|\tilde{\mathcal{T}}_{(x,+,-)}(\omega)|^2$, since it is just one of the T matrices discussed above. We can summarize how the behaviors of the other three functions arise algebraically as follows. As seen in Fig. 2, $\mathrm{Re}(G^{PSF}+T^{++})$ is higher below than above the exciton resonance. This asymmetry is partially compensated for by the concentration of

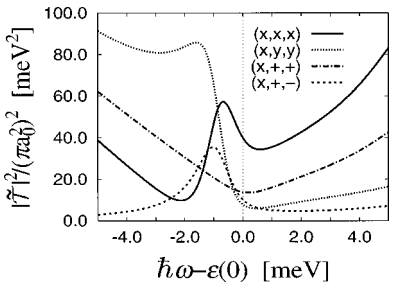

FIG. 7. Interaction-dependent part of the FWM signals: the T matrix (plus G^{PSF}) squared for various polarization configurations.

$\mathrm{Im}(T^{++})$ above $\varepsilon(\mathbf{0})$ to give the resulting shape of $|\tilde{\mathcal{T}}_{(x,+,+)}(\omega)|^2$. $\mathrm{Re}(G^{PSF}+T^{++})$ is positive over the whole energy range, while $\mathrm{Re}(T^{+-}(2\omega))$ crosses from negative to positive around the biexciton energy. Equation (3.4) then implies that this asymmetry suppresses $|\tilde{\mathcal{T}}_{(x,x,x)}(\omega)|^2$, but boosts $|\tilde{\mathcal{T}}_{(x,y,y)}(\omega)|^2$, below half the biexciton energy compared to above the exciton resonance. This trend is reinforced (partially offset) for $|\tilde{\mathcal{T}}_{(x,x,x)}|^2$ ($|\tilde{\mathcal{T}}_{(x,y,y)}|^2$) by the concentration of the imaginary parts on the high-energy side.

Combining the functional behaviors of $D(\omega,\Delta)$ and $|\tilde{\mathcal{T}}_{(\sigma_p,\sigma_t,\sigma_s)}(\omega)|^2$ in Fig. 7, we can easily understand the variations of the FWM signals. A sharper assessment of the contributions from various processes can be obtained by omitting selective terms from the expressions for T^{ij} in the calculations. First, it has long been realized that omitting Coulomb correlations among the excitons, i.e., including only the Hartree-Fock and phase-space filling terms, results in identical FWM signals in the (x,x,x), (x,y,y), and $(x,+,+)$ configurations and no signal in $(x,+,-)$. Less obvious is the differentiation of the signatures of the several types of correlations. From the above considerations, we expect switching off the bound biexciton would reduce the strength at the lower polariton peak in the $(x,+,-)$ configuration and would reduce the difference between the signals in the (x,x,x) and the (x,y,y) configurations. Switching off the excitation-induced dephasing (EID) ($\mathrm{Im}\,T^{++}$ and the continuum part of $\mathrm{Im}\,T^{+-}$) would reduce the signal strength at the upper polariton peak for all configurations. These expectations are confirmed by the results shown in Figs. 8 and 9. The importance of the bound biexciton for the $(x,+,-)$ configuration has also been pointed out in Refs. 30 and 31. Switching off the real part of the continuum T^{ij} leads to some changes in the signals compared to the full calculations (Fig. 10), but, while these changes can be traced in detail back to the features of the T matrix, they can not be easily summarized. In sum, within the present model, good agreement with the experiment is achieved only if all the many-body effects are included.

Among the ingredients of $\chi^{(3)}$, the Hartree-Fock, phase-space filling are easily calculated, and wave functions for the bound biexciton are available in the literature (e.g., Ref. 69). They can also be set in parametrized form with one or two parameters in each to be fitted to experiments. By contrast, a proper calculation of the exciton-exciton continuum correlations involves at least the computational effort as that in the

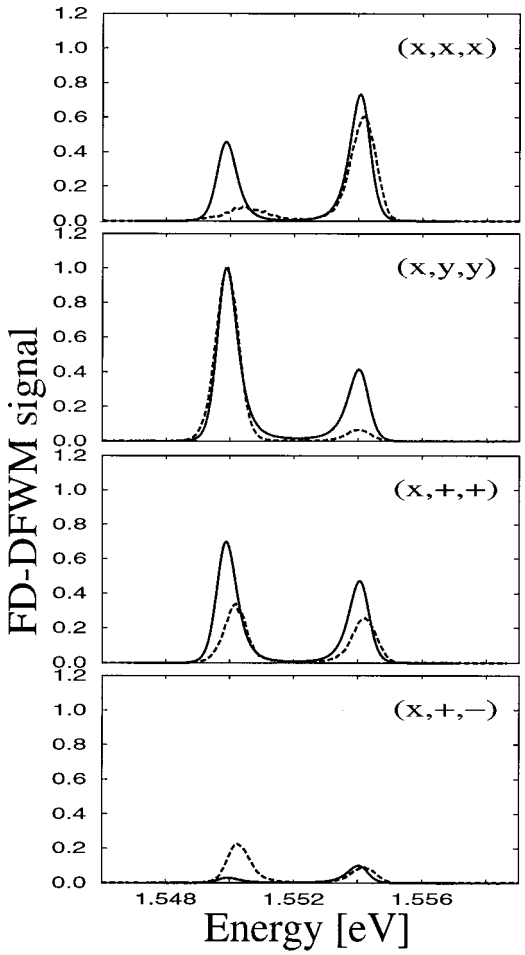

FIG. 8. Comparison between theory (solid line) and experiment (dashed line) for FWM signals at zero detuning. The theoretical signals are calculated without the contributions from the bound biexciton (cf. Fig. 6).

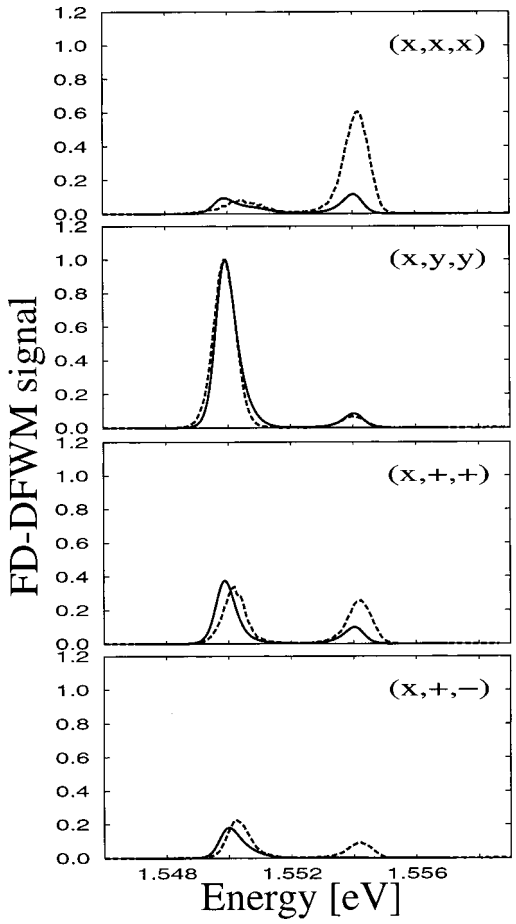

FIG. 9. Comparison between theory (solid line) and experiment (dashed line) for FWM signals at zero detuning. The theoretical signals are calculated without the contributions from EID, or the continuum part of $\mathrm{Im}\, G^{\pm}$ (cf. Fig. 6).

calculation reported in this paper. A natural question is: can the continuum correlations be reliably estimated using some simple approximations, e.g. the second Born or the Markov? In other words, are the experiments under considerations sufficiently sensitive to the correlated-exciton dynamics beyond those captured in these approximations? We have already discussed the effects of each of these approximations on the T matrix in Sec. II B. To examine the question of measurability, we have calculated the corresponding FWM signals. As shown for zero detuning in Fig. 11, the results with the second-Born approximation deviate quite drastically from both the experimental data and the full calculations. The worst effect of taking this approximation is a large spurious transfer of signal strength from the lower polariton peak to the upper one (with some additional enhancement) in the $(x,+,+)$ configuration. This basically results from the strong variation of $\mathrm{Re}\, G^{+}(2\omega)$ at low energy [$\hbar\omega$ close to $\varepsilon(\mathbf{0})$], which, as discussed in Sec. II B, comes with the strong low-energy peak in $\mathrm{Im}\, G^{+}(2\omega)$. Another sizable discrepancy with experiment is the spurious enhancement of the upper peak in the (x,x,x) configuration compared to, say, the lower peak in (x,y,y). The present FWM data thus appear sufficiently sensitive to the energy variations of the Coulomb correlations between two continuum excitons to distinguish between a correct calculation of the scattering matrix and its lowest-order (first and second) perturbative approximations. The Markov approximation to the continuum part of the T matrix was discussed in Sec. II B, where its major effect was shown to be a reduction of $\mathrm{Im}(T^{ij})$ above the exciton edge. Figure 12 shows its effects on the calculated FWM signals at zero detuning, which, as expected, are similar to those seen above in Fig. 9.

The above results were calculated, as explained in the previous section, with the overlap matrix S in Eqs. (2.15) and (2.16) set to zero. We have also performed the calculations including S, the predicted FWM signals of which are compared to the experiment in Fig. 13. Although the agreement is slightly worse than that in Fig. 6, the predicted signals still give a valid description of the data. In other words, although the T matrices calculated with and without S show some quantitative differences, their energy and polarization dependences are sufficiently similar around the two-exciton con tinuum edge that the experimental data being analyzed do not conclusively favor either one.

The results presented in this section clearly show that our microscopic and fermionic description of exciton correlations in the third-order FWM signal of quantum-well micro-

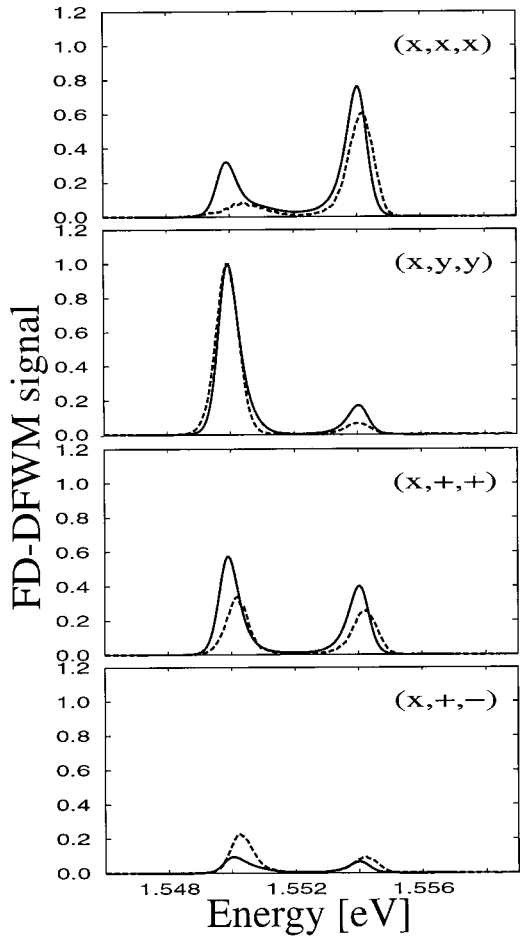

FIG. 10. Comparison between theory (solid line) and experiment (dashed line) for FWM signals at zero detuning. The theoretical signals are calculated without the contributions from the continuum parts of $\mathrm{Re}G^{\pm}$ (cf. Fig. 6).

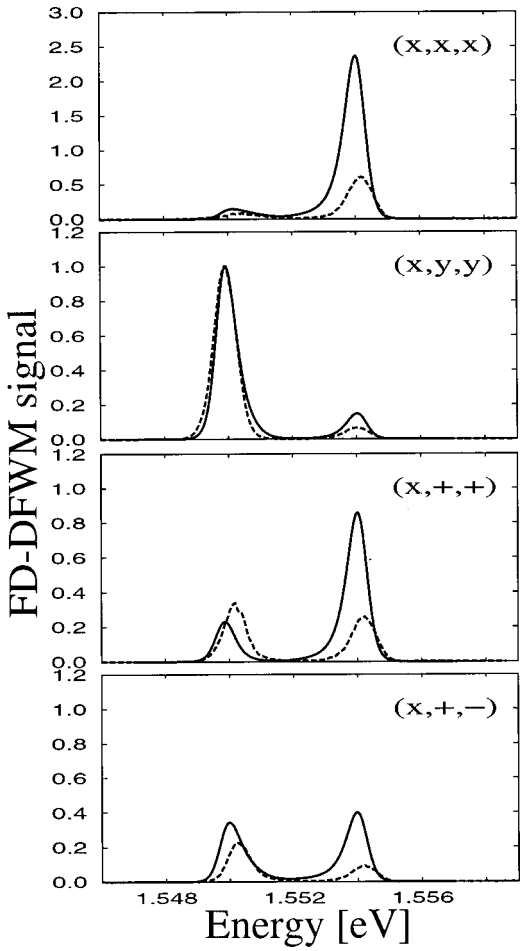

FIG. 11. Comparison between theory (solid line) and experiment (dashed line) for FWM signals at zero detuning. The theoretical signals are calculated in the second-Born approximation to the continuum parts of the T matrix (cf. Fig. 6).

cavities can explain the considered experimental data. It allows for a detailed analysis of the relative weight of the various many-body effects (excitonic phase-space filling, excitonic Hartree-Fock, exciton-exciton correlations including biexcitons) for different polarization configurations.

In the remainder of the section, we critically review the most important assumptions and approximations we have taken in our theory in order to make it computationally tractable and otherwise simpler. They are: (1) The classical treatment of the radiation field, (2) including only *coherent* processes and truncating the resulting DCT hierarchy of equations to third order in the external field, (3) the use of a zero-width model for the quantum well, (4) neglecting all valence bands other than the highest heavy-hole subband and band-mixing effects, and (5) the restriction of the four-fermion Hilbert space to the subspace of two 1s heavy-hole (hh)-excitons in solving the third-order DCT equations.

The $\chi^{(3)}$ DCT equations strongly coupled to a *quantized* cavity radiation field has been formulated,[70,71] but applications at the same detailed quantitative level as the present work appear not to have been attempted. Improvements and extensions of our theory along these lines are now being considered. At this point, we just note that the good agreement, displayed here and elsewhere, achieved between theories based on the semiclassical approaches and experiments suggests that the quantized-field effects may not be important for these experiments. For works on other aspects of quantized-field effects in coherent semiconductor optics, see e.g., Ref. 72 and references therein.

Neglecting incoherent as well as higher order (in the applied field) processes are generally considered justified when the field strength is sufficiently low. Adopting a more realistic finite-width model of the QW and/or a more realistic band structure (see e.g., Ref. 73,74) would introduce changes in the ''input ingredients'' to our theory: basically the exciton binding energy and the exciton wave function(s) used in the calculation of the matrix elements. While these improvements on our theory are not likely to change the qualitative behavior of the T matrices, quantitative effects are to be expected, the magnitude of which is unfortunately not easy to estimate at this point. As for the optical selection rules used in our simplified model, we note that they are consistent with the selection rules obtained within a spherical model, but including all band-coupling and Coulomb-correlation effects within the $\chi^{(3)}$ regime.[75]

The truncation to the 1s hh-subspace is perhaps the most

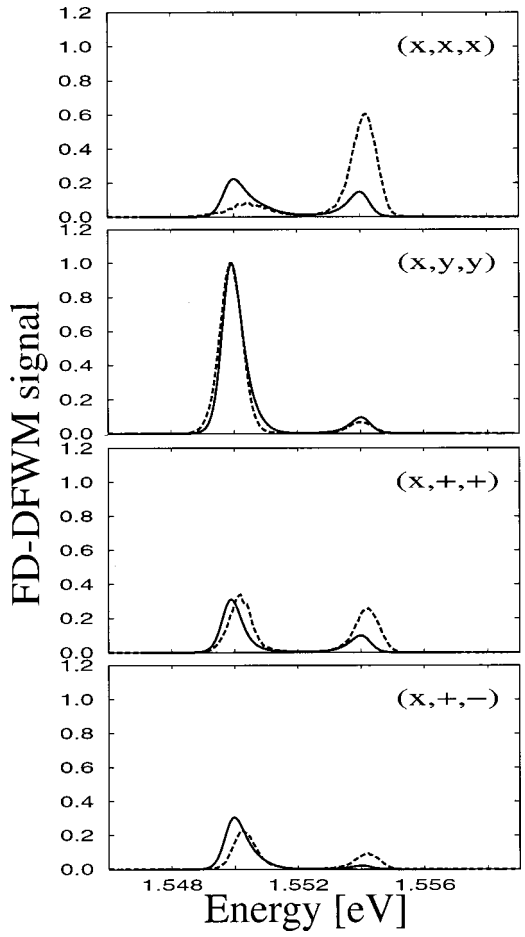

FIG. 12. Comparison between theory (solid line) and experiment (dashed line) for FWM signals at zero detuning. The theoretical signals are calculated in the Markov approximation to the continuum parts of the T matrix (cf. Fig. 6).

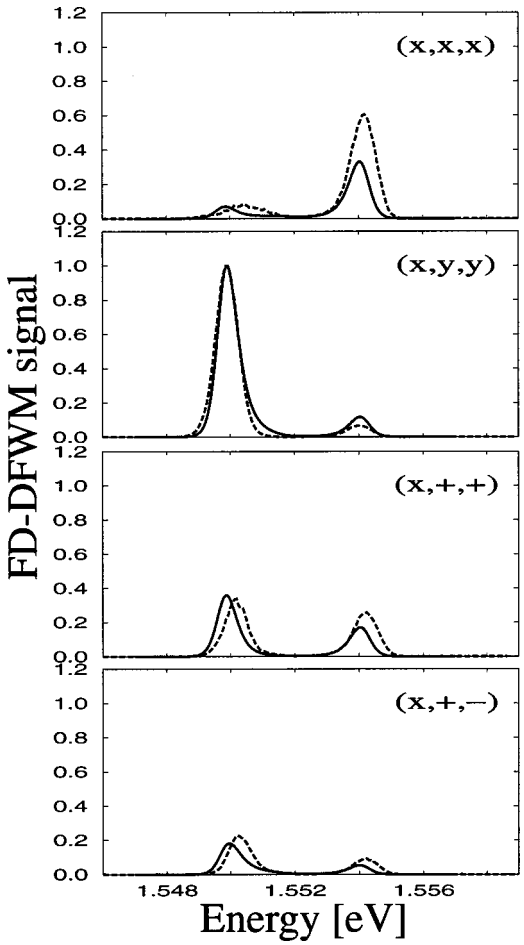

FIG. 13. Comparison between theory (solid line) and experiment (dashed line) for FWM signals at zero detuning. The theoretical signals are calculated with the overlap matrix S included in Eqs. (2.16) and (2.21) (cf. Fig. 6).

drastic approximation taken here. All $1s$ states, including optically inactive ones, are included in the sum over intermediate states in the T matrix. The contributions from all other exciton eigenstates are neglected. Our numerical studies, to be reported in Ref. 49, show the (first-order) coupling between the $1s$ state and other exciton states to be small, which justifies the truncation to a certain extent. Also because of the truncation, inclusion of the overlap matrix S can be problematic. As discussed above, we set it to zero here. Another known defect of the truncation is the underestimation of the biexciton binding energy: the calculated binding energy here is only $\approx 70\%$ percent of the best variational estimate.[76] We have discussed the consequence of this underestimation to the comparison with experiment in Sec. III. These issues can only be sorted out satisfactorily when results of calculations in the full $(2e,2h)$ Hilbert space, performed to the same numerical accuracy as our calculations, are available for comparison. The key features of the FWM signals that we have identified are likely to be independent of this approximation.

IV. SUMMARY

We have presented a microscopic theory of third-order degenerate four-wave-mixing response of a quantum well in a microcavity around the lowest exciton resonance. It consists of a classical treatment of the radiation field coupled to a coherent dynamics-controlled-truncation (DCT) treatment of the quantum many-electron-hole system. Truncating the DCT equations to the heavy-hole $1s$-exciton subspace, we arrived at an effective exciton-exciton scattering theory, expressing the $\chi^{(3)}$ susceptibility in terms of an off-energy-shell exciton scattering (or T) matrix. Owing to the dimensionality $(=2)$ of the system, the T matrix is highly nonperturbative around the exciton-exciton continuum edge, necessitating an exact diagonalization of the $1s$-exciton Hamiltonian for its calculation. The failure of two common approximations, second Born and Markov, were discussed.

The theory presented here yields predictions for the polarization dependence of the FWM signals as well as the relative signal strengths at the two polariton peaks. These predictions are in quantitative agreement with the experimental data reported in Refs. 14,18. Such a quantitative comparison allows unambiguous identification of many-particle correlations, including both biexciton and two-exciton continuum scattering.

Our discussions have also identified issues to be resolved in the future, which include the effect of the quantized nature

of the photon and that of the higher-excitonic states on the $1s$-exciton scattering. The latter is especially important if we wish to extend the validity of our present theory to higher light frequencies.

ACKNOWLEDGMENTS

This work was supported by grants from NSF (Division of Materials Research), JSOP, COEDIP (University of Arizona). We thank W. Schäfer for sending us part of his book (Ref. 29) prior to publication and Y.P. Svirko and R. Shimano for useful discussions.

APPENDIX A: RADIATION FIELD IN THE QUANTUM-WELL MICROCAVITY

In this appendix, we summarize the calculations of the electric field inside the QW and the enhancement factors relating the field inside the QW to that outside the cavity. The treatment here will be brief, more detailed explanations of the methods being readily available in the standard references (see, e.g., Ref. 3 and references therein).

We start with some notational conventions. The z coordinates of the cavity's left end, the cavity's right end, the QW's left end, and the QW's right end are labeled $z_t^{\pm}$, $z_b^{\pm}$, $z_0^{\pm}$, and $z_1^{\pm}$, respectively. The superscript $+(-)$ denotes the right(left) side of the interface at the point in question (Fig. 1). In Sec. II A, the electric field inside the QW has been expanded perturbatively in the externally applied field. The first and third-order terms are to be obtained as the solutions to Eqs. (2.5) and (2.6) respectively. First we fix the confinement wave function as simply $|\xi(z)|^2=1/L$, where L is the well width. For sufficiently small L, which is the case here, the third-order susceptibility that results is not sensitive to the specific choice of this wave function. Being a linear equation, Eq. (2.5) is easily solved (e.g. by Green's function). Its general solution may be written as

$$\mathbf{E}^{(1)}(z,\omega)=\mathbf{E}^{(1)+}(z_0^+,\omega)\exp\{ik_Q(z-z_0^+)\}-\mathbf{E}^{(1)-}(z_0^+,\omega)\exp\{-ik_Q(z-z_0^+)\}+\frac{4\pi}{n_b^2 L}\chi^{(1)}(\omega)\mathbf{E}_Q^{(1)}(\omega)[\cos(k_Q(z-z_0^+))-1], \tag{A1}$$

where $k_Q=n_b\omega/c$. The solution depends on two undetermined parameters $\mathbf{E}^{(1)+}(z_0^+,\omega)$ and $\mathbf{E}^{(1)-}(z_0^+,\omega)$ that give the field and its z derivative at z_0^+, the left end of the QW. By integrating both sides of Eq. (A1) over z, the averaged field over the QW is obtained to be

$$\mathbf{E}_Q^{(1)}(\omega)=\frac{\mathbf{E}^{(1)+}(z_0^+,\omega)\{\exp[ik_Q(z-z_0^+)]-1\}+\mathbf{E}^{(1)-}(z_0^+,\omega)\{\exp[-ik_Q(z-z_0^+)]-1\}}{ik_QL\left[1+\frac{4\pi}{n_b^2L}\chi^{(1)}(\omega)\left(1-\frac{\sin(k_QL)}{k_QL}\right)\right]}. \tag{A2}$$

Using $\mathbf{E}_Q^{(1)}(\omega)$ as the driving field for the third order DCT equation in Sec. II B, we obtain the source term $[\chi^{(3)}\mathbf{E}_Q^{(1)}\mathbf{E}_Q^{(1)}\mathbf{E}_Q^{(1)*}]$ to Eq. (2.6), which may again be solved in the same way as Eq. (2.5). The solution, which we do not write down here, is used to calculate the $\chi^{(3)}$ enhancement factor below.

The propagation of the electric field through the DBR's and the spacer layers are treated by the standard transfer matrix formalism. As solution to the Maxwell wave equation, the electric field in each dielectric layer, with refractive index n, is written as

$$\mathbf{E}(z,\omega)=\mathbf{E}^+(\bar{z},\omega)e^{ik(z-\bar{z})}-\mathbf{E}^-(\bar{z},\omega)e^{-ik(z-\bar{z})}, \tag{A3}$$

where $k=n\omega/c$ and $\mathbf{E}^+(\bar{z},\omega)$ and $\mathbf{E}^-(\bar{z},\omega)$ are, respectively, the right and left going field amplitudes at an arbitrary point $\bar{z}$ inside the layer. Written as a column vector, these field amplitudes are related to those in other layers by 2×2 matrices that depend only on the material parameters. Referring to Fig. 1, at the interface between two dielectric layers, with refractive index n_1 (n_2) on the left (right) say, the transfer matrix $\mathcal{M}_{21}$ relating the field amplitudes on the right to those on the left of the interface is

$$\begin{pmatrix}\mathbf{E}_R^+\\ \mathbf{E}_R^-\end{pmatrix}=\mathcal{M}_{21}\begin{pmatrix}\mathbf{E}_L^+\\ \mathbf{E}_L^-\end{pmatrix},\quad \mathcal{M}_{21}=\frac{1}{2}\begin{pmatrix}\frac{n_1}{n_2}+1 & \frac{n_1}{n_2}-1\\ \frac{n_1}{n_2}-1 & \frac{n_1}{n_2}+1\end{pmatrix}. \tag{A4}$$

Another matrix: $\mathcal{N}_j=\mathrm{diag}(e^{ik_jd_j},e^{-ik_jd_j})$, propagates the field amplitudes across (from left to right) a dielectric layer of width d_j and refractive index n_j, with $k_j=n_j\omega/c$. The transfer matrix between any two layers in a DBR can be constructed as a product of these $\mathcal{M}$'s and $\mathcal{N}$'s. The propagation through the QW has the added complication of the resonant polarization. Denoted by M_{QW}, the transfer matrix that propagates the *first-order* field amplitudes from z_0^- to z_1^+ can be obtained with Eq. (A1) and the interface (dis)continuity conditions. In this work we have only used the $L\to0$ limit of M_{QW}, which is

$$M_{QW}=\begin{pmatrix}1+\beta_r & -\beta_r\\ \beta_r & 1-\beta_r\end{pmatrix},\quad \beta_r=i\frac{2\pi\omega}{n_sc}\chi^{(1)}(\omega), \tag{A5}$$

where n_s is the spacer refractive index. The transfer matrix

propagating the first-order field across the entire QW microcavity M_{CAV} can thus be written as $M_{CAV}=M_B M_{QW} M_T$, where M_T propagates across the left DBR from z_t^- to z_0^- and M_B across the right DBR from z_1^+ to z_b^+. M_T and M_B are products of $\mathcal{M}$'s and $\mathcal{N}$'s as explained above. M_{CAV} represents two linear equations, the solution of which is fixed by two boundary conditions at the ends of the cavity: the incoming field on the left side is the applied field, and there is no incoming field on the right side. With the solution, the linear enhancement factor $C^{(1)}$, relating the field average inside the QW $\mathbf{E}_Q^{(1)}$ to the incident field $\mathbf{E}_0$, is given by

$$C^{(1)}(\omega)=t_{11}-t_{21}-\frac{m_{21}}{m_{22}}(t_{12}-t_{22}), \tag{A6}$$

where t_{ij} and $m_{ij}, i,j=1,2$ are the elements of M_T and M_{CAV}, respectively.

The solution to Eq. (2.6) gives the connection between the third-order field amplitudes outside the two ends of the QW, which again in the $L\to 0$ limit, is given by

$$\begin{pmatrix} \mathbf{E}^{(3)+}(z_1^+) \\ \mathbf{E}^{(3)-}(z_1^+) \end{pmatrix} = M_{QW} \begin{pmatrix} \mathbf{E}^{(3)+}(z_0^-) \\ \mathbf{E}^{(3)-}(z_0^-) \end{pmatrix} + \frac{2\pi\omega}{n_s c} i[\chi^{(3)} \mathbf{E}_Q^{(1)} \mathbf{E}_Q^{(1)} \mathbf{E}_Q^{(1)*}] \begin{pmatrix} 1 \\ 1 \end{pmatrix}. \tag{A7}$$

These amplitudes are again propagated to outside the cavity by M_T and M_B. Since the third-order field originating from inside the QW, the appropriate boundary condition is that of zero incoming field on both ends. The cubic enhancement factors C_r and C_t, relating the third order fields outside the cavity, $\mathbf{E}_r^{(3)}(z_t^-,\omega)$ and $\mathbf{E}_t^{(3)}(z_b^+,\omega)$ respectively, to the third order interband polarization inside the QW, is given by

$$C_r(\omega)=-2\pi i\frac{\omega}{n_s c}\left[\frac{b_{21}+b_{22}}{m_{22}}\right], \tag{A8}$$

$$C_t(\omega)=2\pi i\frac{\omega}{n_s c}\left[b_{11}+b_{12}-\frac{m_{12}}{m_{22}}(b_{21}+b_{22})\right], \tag{A9}$$

where $b_{ij}, i,j=1,2$ are the elements of M_B.

APPENDIX B: COULOMB AND OVERLAP MATRICES

In Eq. (2.15) we wrote the effective-exciton Hamiltonian in terms of the Coulomb matrix $W^{xx(\lambda)}$ and the overlap matrix S. We give the explicit expressions of these matrices in this appendix.

The Hamiltonian is block diagonal in the total electron spin states: $\lambda=+(-)$ for triplet (singlet). In this basis, the Coulomb interaction between two $1s$ excitons from an initial state with relative momentum $\mathbf{q}'$ to a final state with $\mathbf{q}$ is

$$W^{xx(\lambda)}_{\mathbf{q},\mathbf{q}'}=W^{xx(\lambda)}_{\mathbf{q},\mathbf{q}'}|_{direct}+\lambda W^{xx(\lambda)}_{\mathbf{q},\mathbf{q}'}|_{ex}, \tag{B1}$$

where

$$W^{xx}_{\mathbf{q},\mathbf{q}'}|_{direct}=V(\mathbf{q}-\mathbf{q}')M(\mathbf{q}-\mathbf{q}')M(\mathbf{q}'-\mathbf{q})$$

$$\begin{aligned} W^{xx}_{\mathbf{q},\mathbf{q}'}|_{ex}=\sum_{\mathbf{k}\mathbf{k}'} & V(\mathbf{k}-\mathbf{k}')\phi^*(\mathbf{k}+\alpha(\mathbf{q}-\mathbf{q}')) \\ & \times\phi^*[\mathbf{k}'+\beta(\mathbf{q}+\mathbf{q}')][\phi(\mathbf{k})-\phi(\mathbf{k}')] \\ & \times[\phi(\mathbf{k}+\alpha(\mathbf{q}-\mathbf{q}')+\beta(\mathbf{q}+\mathbf{q}')) \\ & -\phi(\mathbf{k}'+\alpha(\mathbf{q}-\mathbf{q}')+\beta(\mathbf{q}+\mathbf{q}'))]. \end{aligned} \tag{B2}$$

Here $\alpha=m_h/(m_e+m_h)$, $\beta=m_e/(m_e+m_h)$, and $\phi(\mathbf{k})$ is the $1s$-exciton wave function. In the direct term, the so-called excitonic transition element is given by

$$M(\mathbf{q})=\sum_{\mathbf{k}}\phi^*(\mathbf{k})[\phi(\mathbf{k}+\beta\mathbf{q})-\phi(\mathbf{k}-\alpha\mathbf{q})]. \tag{B3}$$

We note that the direct term goes to zero at low $\mathbf{q}$, leaving the exchange term mostly responsible for the low-energy behavior of the T matrix discussed in Sec. II B. Finally, the overlap matrix element is

$$\begin{aligned} S_{\mathbf{q},\mathbf{q}'}=\sum_{\mathbf{k}} & \phi^*(\mathbf{k}+\alpha\mathbf{q})\phi^*(\mathbf{k}+\mathbf{q}'+\beta\mathbf{q})\phi(\mathbf{k}+\alpha\mathbf{q}')\phi \\ & \times(\mathbf{k}+\mathbf{q}+\beta\mathbf{q}'). \end{aligned} \tag{B4}$$

[1] H. Yokoyama and K. Ujihara, *Spontaneous Emission and Laser Oscillation in Microcavities* (CRC Press, New York, 1995).

[2] C. Weisbuch, M. Nishioka, A. Ishikawa, and Y. Arakawa, Phys. Rev. Lett. **69**, 3314 (1992).

[3] G. Khitrova, H. M. Gibbs, F. Jahnke, M. Kira, and S. W. Koch, Rev. Mod. Phys. **71**, 1591 (1999).

[4] Y. Chen, A. Tredicucci, and F. Bassani, J. Phys. IV **3**, 453 (1993).

[5] D. Citrin, IEEE J. Quantum Electron. **30**, 997 (1994).

[6] S. Jorda, Phys. Rev. B **50**, 2283 (1994).

[7] S. Jorda, Phys. Rev. B **49**, 8774 (1994).

[8] C. Ell, J. Prineas, J. T. R. Nelson, S. Park, H. M. Gibbs, G. Khitrova, S. W. Koch, and R. Houdre, Phys. Rev. Lett. **80**, 4795 (1998).

[9] G. Panzarini, L. C. Andreani, A. Armitage, D. Baxter, M. S. Skolnick, V. N. Astratov, J. S. Roberts, A. V. Kavokin, M. R. Vladimirova, and M. A. Kaliteevski, Phys. Solid State **41**, 1223 (1999).

[10] R. Houdre, C. Weisbuch, R. P. Stanley, U. Oesterle, and M. Ilegems, Photonics Spectra **7**, 625 (2000).

[11] R. Huang, F. Tassone, and Y. Yamamoto, Phys. Rev. B **61**, R7854 (2000).

[12] C. Wilmsen, H. Temking, and L. Coldren, *Vertical-cavity Surface-emitting Lasers: Design, Fabrication, Characterization, and Applications* (Cambridge University Press, Cambridge, 1999).

[13] F. Quochi, G. Bongiovanni, A. Mura, J. L. Staehli, B. Deveaud,

R. P. Stanley, U. Oesterle, and R. Houdre, Phys. Rev. Lett. **80**, 4733 (1998).
[14] M. Kuwata-Gonokami, S. Inoue, H. Suzuura, M. Shirane, and R. Shimano, Phys. Rev. Lett. **79**, 1341 (1997).
[15] H. Suzuura, Y. Svirko, and M. Kuwata-Gonokami, Solid State Commun. **108**, 289 (1998).
[16] H. Wang, H. Q. Hou, and B. E. Hammons, Phys. Rev. Lett. **81**, 3255 (1998).
[17] H. Fan, H. Wang, H. Q. Hou, and B. E. Hammons, Phys. Rev. B **57**, R9451 (1998).
[18] M. Shirane, C. Ramkumar, Y. P. Svirko, H. Suzuura, S. Inoue, R. Shimano, T. Someya, H. Sakaki, and M. Kuwata-Gonokami, Phys. Rev. B **58**, 7978 (1998).
[19] Y. P. Svirko, M. Shirane, H. Suzuura, and M. Kuwata-Gonokami, J. Phys. Soc. Jpn. **68**, 647 (1999).
[20] T. Aoki, G. Mohs, and M. Kuwata-Gonokami, Phys. Rev. Lett. **82**, 3108 (1999).
[21] C. Sieh, T. Meier, A. Knorr, F. Jahnke, P. Thomas, and S. W. Koch, Eur. Phys. J. B **11**, 407 (1999).
[22] P. G. Savvidis, J. J. Baumberg, R. M. Stevenson, M. S. Skolnick, D. M. Whittaker, and J. S. Roberts, Phys. Rev. Lett. **84**, 1547 (2000).
[23] M. J. Werner and A. Imamoglu, Phys. Rev. A **61**, 011801 (2000).
[24] C. Ciuti, P. Schwendimann, B. Deveaud, and A. Quattropani, Phys. Rev. B **62**, R4825 (2000).
[25] R. Zimmermann, *Many-Particle Theory of Highly Excited Semiconductors* (Teubner, Leipzig, 1988).
[26] H. Haug and S. W. Koch, *Quantum Theory of the Optical and Electronic Properties of Semiconductors*, 2nd ed. (World Scientific, Singapore, 1993).
[27] J. Shah, *Ultrafast Spectroscopy of Semiconductors and Semiconductor Nanostructures, Springer Series in Solid-State Sciences* Vol. 115 (Springer, Berlin, 1996).
[28] H. Haug and A. P. Jauho, *Quantum Kinetics in Transport and Optics of Semiconductors* (Springer, Berlin, 1996).
[29] W. Schäfer and M. Wegener, *Semiconductor Optics and Transport - From Fundamentals to Current Topics* (Springer, Berlin, in press).
[30] M. Kuwata-Gonokami, T. Aoki, C. Ramkumar, R. Shimano, and Y. Svirko, J. Lumin. **87-89**, 162 (2000).
[31] Y. Svirko and M. Kuwata-Gonokami, Phys. Rev. B **62**, 6912 (2000).
[32] V. M. Axt and A. Stahl, Z. Phys. B: Condens. Matter **93**, 195 (1994).
[33] V. M. Axt and A. Stahl, Z. Phys. B: Condens. Matter **93**, 205 (1994).
[34] M. Lindberg, Y. Z. Hu, R. Binder, and S. W. Koch, Phys. Rev. B **50**, 18 060 (1994).
[35] W. Schäfer, D. Kim, J. Shah, T. Damen, J. Cunningham, K. Goossen, L. Pfeiffer, and K. Köhler, Phys. Rev. B **53**, 16 429 (1996).
[36] P. Kner, S. Bar-Ad, M. V. Marquezini, D. S. Chemla, and W. Schäfer, Phys. Rev. Lett. **78**, 1319 (1997).
[37] V. M. Axt, K. Victor, and T. Kuhn, Phys. Status Solidi B **206**, 189 (1998).
[38] G. Bartels and A. Stahl, Phys. Status Solidi B **206**, 325 (1998).
[39] T. Östreich, K. Schönhammer, and L. Sham, Phys. Rev. B **58**, 12 920 (1998).
[40] G. Bartels, A. Stahl, V. Axt, B. Haase, U. Neukrich, and J. Gutowski, Phys. Rev. B **81**, 5880 (1998).
[41] T. Östreich and L. J. Sham, Phys. Rev. Lett. **83**, 3510 (1999).
[42] C. Sieh, T. Meier, F. Jahnke, A. Knorr, S. Koch, P. Brick, M. Hübner, C. Ell, J. Prineas, G. Khitrova, and H. Gibbs, Phys. Rev. Lett. **82**, 3112 (1999).
[43] R. Binder and S. Koch, Prog. Quantum Electron. **19**, 307 (1995).
[44] F. Jahnke, M. Kira, and S. Koch, Z. Phys. B: Condens. Matter **104**, 559 (1997).
[45] D. Burak and R. Binder, IEEE J. Quantum Electron. **33**, 1205 (1997).
[46] R. Shimano, S. Inouye, M. Kuwata-Gonokami, T. Nakamura, M. Yamanishi, and I. Ogura, Jpn. J. Appl. Phys., Part 2 **34**, L817 (1995).
[47] V. M. Axt, K. Victor, and A. Stahl, Phys. Rev. B **53**, 7244 (1996).
[48] V. M. Axt and S. Mukamel, in *Nonlinear Optic Materials*, edited by J. V. Moloney (Springer, New York, 1998).
[49] R. Takayama *et al.* (unpublished).
[50] In the case of Frenkel excitons, the fact that ''the scattering amplitude should have some direct signatures in $\chi^{(3)}$'' was noted in: V. Chernyak, S. Yokojima, T. Meier, and S. Mukamel, Phys. Rev. B **58**, 4496 (1998).
[51] R. G. Newton, *Scattering Theory of Waves and Particles* (Springer, New York, 1982).
[52] V. N. Popov, *Functional Integrals in Quantum Field Theory and Statistical Physics* (Reidel, Dordrecht, 1983).
[53] For example, ε_c can be used to estimate the transition temperature to the superfluid state.[52]
[54] N. H. Kwong, R. Takayama, I. Rumyantsev, M. Kuwata-Gonokami, and R. Binder, Phys. Rev. Lett. (to be published).
[55] In addition to the example cited in Ref. 53 see also M. Schick, Phys. Rev. A **3**, 1067 (1971), which shows how to obtain, among other things, the chemical potential of an interacting 2D Bose gas at zero temperature from the *T* matrix.
[56] L. Banyai, Q. Vu, and H. Haug, Phys. Rev. B **58**, R13 341 (1998).
[57] S. Haas, T. Stroucken, M. Hubner, J. Kuhl, B. Grote, A. Knorr, F. Jahnke, S. W. Koch, R. Hey, and K. Ploog, Phys. Rev. B **57**, 14 860 (1998).
[58] O. M. Schmitt, I. Banyai, and H. Haug, J. Lumin. **87**, 168 (2000).
[59] H. Wang, K. Ferrio, D. Steel, Y. Hu, R. Binder, and S. Koch, Phys. Rev. Lett. **71**, 1261 (1993).
[60] A. C. Schaefer and D. G. Steel, Phys. Rev. Lett. **79**, 4870 (1997).
[61] H. P. Wagner, A. Schatz, R. Maier, W. Langbein, and J. M. Hvam, Photonics Spectra **2**, 82 (1998).
[62] H. P. Wagner, A. Schatz, R. Maier, W. Langbein, and J. M. Hvam, Phys. Rev. B **57**, 1791 (1998).
[63] H. P. Wagner, A. Schätz, W. Langbein, J. M. Hvam, and A. L. Smirl, Phys. Rev. B **60**, 4454 (1999).
[64] G. R. Allan and H. M. van Driel, Phys. Rev. B **59**, 15 740 (1999).
[65] A. L. Smirl, in *Semiconductor Quantum Electronics: From Quantum Physics to Smart Devices*, edited by A. Miller, M. Ebrahimzadeh, and D. M. Finlayson (IOP Publishing, Bristol, 1974), p. 25.
[66] A. L. Smirl, M. J. Stevens, X. Chen, and O. Buccafusca, Phys. Rev. B **60**, 8267 (1999).
[67] T. Baars, M. Bayer, A. Forchel, F. Schaefer, and J. Reithmaier, Phys. Rev. B **61**, R2409 (2000).
[68] W. Langbein and J. M. Hvam, Phys. Rev. B **61**, 1692 (2000).
[69] D. A. Kleinman, Phys. Rev. B **28**, 871 (1983).

[70] S. Savasta and R. Girlanda, Phys. Rev. Lett. **77**, 4736 (1996).
[71] S. Savasta and R. Girlanda, Phys. Rev. B **59**, 15 409 (1999).
[72] M. Kira, F. Jahnke, W. Hoyer, and S. W. Koch, Prog. Quantum Electron. **23**, 189 (1999); M. Kira, F. Jahnke, and S. W. Koch, Phys. Rev. Lett. **82**, 3544 (1999).
[73] J. N. Shulman and Y. C. Chang, Phys. Rev. B **31**, 2056 (1985).
[74] L. Andreani and A. Pasquarello, Phys. Rev. B **42**, 7641 (1990).
[75] M. Lindberg, R. Binder, Y. Z. Hu, and S. W. Koch, Phys. Rev. B **49**, 16 942 (1994).
[76] Y. Suzuki and K. Varga, *A Stochastic Variational Approach to Quantum-mechanical Few-body Problems* (Springer, Berlin, 1998).